

Entanglements in a Quiescent and Sheared Polymer Melt

Ryoichi Yamamoto and Akira Onuki

Department of Physics, Kyoto University, Kyoto 606-8502, Japan

(November 10, 2018)

Molecular dynamics simulations were performed for a polymer melt. In quiescent states the inter-chain interaction energy supported by each particle takes relatively large values persistently for long times if the particle is close to an entanglement. Thus, if the interaction is averaged over appropriate time intervals, we can detect active spots on the chains produced by entanglement constrains. If rapid shearing is applied, these active regions subsequently become bended in eventual zig-zag shapes of the chains. We also demonstrate that stress overshoot occurs with onset of disentanglement.

PACS numbers: 83.10.Nn, 83.20.Jp, 83.50.By, 61.25.Hq

The dynamics of dense polymer melts has been a challenging subject in current polymer physics [1,2]. While the dynamics of short chains can be reasonably described by the simple Rouse model, the dynamics of very long chains has not yet been well understood on the microscopic level since it is governed by entanglement effects. The reptation theory [1,2] is the most successful approach to date in describing the dynamics of entangled polymer chains. It has been supported by a number of experimental and numerical works [3–10], where experimentally accessible quantities such as the stress relaxation function $G(t)$, the incoherent dynamic scattering function, and the mean square displacement have been compared with the theoretical predictions. Understanding rheological properties of polymer melts is also of great importance and extensive simulations have been performed in this direction [9–11]. In a unique paper, Ben-Naim *et al.* [12] could visualize individual entanglements using the fact that incidental contacts of the particles and entanglement contacts behave differently because entanglement constraints are long-lived. The main motivation of our simulation is to identify entanglements more systematically on the microscopic level and examine how they influence rheology in rapid shearing.

We used the bead-spring model [4] for our polymer melt composed of M chains with N beads. All the bead particles interact via the Lennard-Jones potential, $U_{\text{LJ}}(r) = 4\epsilon[(\sigma/r)^{12} - (\sigma/r)^6] + \epsilon$, truncated at the minimum distance $2^{1/6}\sigma$. It serves to prevent spatial overlap of the particles. In addition, bonded pairs or consecutive beads on each chain are connected by an anharmonic spring potential of the form, $U_{\text{FENE}}(r) = -\frac{1}{2}k_c R_0^2 \ln[1 - (r/R_0)^2]$ with $k_c = 30\epsilon/\sigma^2$ and $R_0 = 1.5\sigma$. As a result, the bond lengths deviate within only a few % from the minimum of $U_{\text{LJ}}(r) + U_{\text{FENE}}(r)$ given by 0.96σ . The number density and temperature were fixed at $n = NM/V = 1/\sigma^3$ and $T = \epsilon/k_B$. We measure space and time in units of σ and $\tau_0 = (m\sigma^2/\epsilon)^{1/2}$ with m being the bead mass. We numerically solved the Newton's equation of motion and took data after long equilibration periods of order 10^6 to avoid aging (slow equilibration).

In quiescent cases, we imposed the micro-canonical condition with the time step $\Delta t = 0.005$ for numerical integration. In order to obtain accurate linear viscoelastic behavior of entangled polymers, very long simulations of order $10\tau_d$ were performed for a system composed of $M = 10$ chains each consisting of $N = 250$ beads, where $\tau_d = 6 \times 10^5$ is the stress relaxation time. In the presence of shear flow, we set $\Delta t = 0.0025$ and kept the temperature at a constant using the Gaussian constraint thermostat to eliminate viscous heating. After a long equilibration time in a quiescent state for $t < 0$, all the particles acquired a velocity $\dot{\gamma}y$ in the x direction at $t = 0$, and then the Lee-Edwards boundary condition [13,14] maintained the simple shear flow for $t > 0$. Steady sheared states were realized after transient nonlinear viscoelastic regime.

First, we show data of the stress relaxation function,

$$G(t) = \langle P_{xy}(t)P_{xy}(0) \rangle / V k_B T, \quad (1)$$

at zero shear rate in Fig.1, where P_{xy} is the xy component of the total stress tensor. For the shorter chain case of $N = 25$ and $M = 40$, $G(t)$ is well fitted to the Rouse relaxation function [15], $G_R(t) = (nk_B T/N) \sum_{p=1}^{N-1} \exp(-t/\tau_p)$, where $\tau_p = \tau_{01} / \sin^2(p\pi/2N)$ with $\tau_{01} = \zeta b^2 / 12k_B T \cong 6.5$ [16]. $G(t)$ for the longer chain case of $N = 250$ and $M = 10$ was obtained from a single extremely long simulation ($\sim 5 \times 10^6 = 10^9 \Delta t$). It clearly exhibits slow relaxation due to entanglements. Indeed, it can reasonably well be fitted to the stress relaxation function from the reptation theory, $G_{\text{rep}}(t) = (8nk_B T/\pi^2 N_e) \sum_{p=\text{odd}} \exp(-p^2 t/\tau_d) / p^2$, with $N = 250$, $N_e = 100$, and $\tau_d = 6 \times 10^5$ for $t \gtrsim 2 \times 10^5$.

In order to identify and visualize entanglements for the case $N = 250$, we define the potential energy of non-bonded interaction on the i -th particle by

$$E_i^{\text{NB}}(t) = \sum_{j \in \text{non bond}} U_{\text{LJ}}(|\mathbf{r}_i(t) - \mathbf{r}_j(t)|), \quad (2)$$

where the particle j is not bonded to i . The distribution of $E_i^{\text{NB}}(t)$ at each time t is nearly Gaussian, and there is no appreciable correlation even between adjacent beads,

because $E_i^{\text{NB}}(t)$ consists mostly of rapidly varying thermal fluctuations. To eliminate the rapid components we examine its time average,

$$\bar{E}_i^{\text{NB}}(t) = \frac{1}{\tau} \int_0^\tau dt' E_i^{\text{NB}}(t+t'), \quad (3)$$

where the time interval τ is much longer than 1. We find that the variance,

$$\sigma(\tau) = \sqrt{\frac{1}{MN} \sum_i \left(\bar{E}_i^{\text{NB}} - \langle \bar{E}^{\text{NB}} \rangle \right)^2}, \quad (4)$$

decreases as $\tau^{-1/2}$ with increasing τ in the region $1 \ll \tau \ll \tau_d$, where $\langle \bar{E}^{\text{NB}} \rangle$ is the average. This is because the rapidly varying contributions behave as white-noises. With this time-averaging procedure, strong correlations due to entanglements become apparent in the non-bonded interactions along the chains. Fig.2 displays instantaneous values E_i^{NB} in (a) and time-averaged values \bar{E}_i^{NB} with $\tau = 5 \times 10^3$ in (b). The chains are straightened horizontally for the visualization purpose. While no correlations can be seen in (a), we can see active spots which consist of several consecutive beads having distinctly large values of \bar{E}_i^{NB} . Then we recognize that there are two or three entanglements on each chain. Furthermore, to examine the correlations in \bar{E}_i^{NB} along the chains quantitatively, we define the auto-correlation function,

$$C(n) = \frac{1}{\mathcal{N}} \sum_{j-i=n} \left(\bar{E}_i^{\text{NB}} - \langle \bar{E}^{\text{NB}} \rangle \right) \left(\bar{E}_j^{\text{NB}} - \langle \bar{E}^{\text{NB}} \rangle \right), \quad (5)$$

where the two beads i and j are separated by n on the same chain. The normalization factor \mathcal{N} is defined such that $C(0) = 1$; then, $\mathcal{N} = MN\sigma(\tau)^2$. In Fig.3, we show $C(n)$ in (a) and its power spectrum,

$$P(k) = \sum_{n=0}^{N-1} C(n) \exp(-ikn), \quad (6)$$

in (b) for various τ in the range $0 \leq \tau \ll \tau_d$. The correlation between adjacent beads $C(1)$ is nearly zero for $\tau = 0$ but increases with increasing τ . The decay of $C(n)$ for $n \lesssim 10$ becomes slower with increasing τ . The width Δn determined by $C(\Delta n) \lesssim 10^{-2}$ in Fig.3a grows with increasing τ roughly as $\Delta n \propto \tau^a$ with $a \simeq 0.35$. This widening arises from the motion of entanglements along the chains or equivalently from the motion of chains through tubes formed by entanglement constraints [1,2]. At $\tau = 5 \times 10^3$, $C(n)$ takes a negative minimum around $n \simeq 45$ and a positive maximum around $n \simeq 80$. Correspondingly, $P(k)$ has a peak at $k \simeq 2\pi/80$. Thus the average bead number N_e between entanglements is about

80, which is consistent with recent simulation results [8]. For much larger τ ($> 5 \times 10^4$), however, no periodic structure of $C(n)$ was observed because entanglements become delocalized along the chains on such very long time scales.

Next, we applied a shear flow with rate $\dot{\gamma} = 10^{-3}$ ($\simeq 500/\tau_d$) using the same initial condition which gave the data shown in Fig.2b. In Fig.4 the chain conformations are projected on the xz plane at $\dot{\gamma}t = 5$ in (a) and $\dot{\gamma}t = 10$ in (b). Because the chains are rapidly elongated, they eventually take zig-zag shapes bended at entanglements. Remarkably, the active regions detected without shear in Fig.2b mostly become bended under shear in Fig.4a. Here we give the same number to an active spot in Fig.2a and that in Fig.4a on the same chain if their distance measured along the chain remains shorter than 10. This coincidence unambiguously demonstrates the validity of the time-averaging method used in Fig.2b to visualize entanglements in quiescent states. Furthermore, the non-bonded interactions in these entangled regions (mostly in bended parts) become increasingly amplified with increasing the strain, obviously because a considerable fraction of the stress is supported by entanglements in strong deformations. As a result, they can be detected even with much smaller τ than in the quiescent condition, so we set $\tau = 500$ in calculating \bar{E}_i^{NB} in Fig.4. From Fig.4a to Fig.4b the movement of the entangled regions could be followed, so the corresponding parts in Fig.4a and Fig.4b can be marked with the same number. We can also see that the total number of these regions has not yet decreased in Fig.4b at $\dot{\gamma}t = 10$, but several of them are approaching chain ends and are going to disappear. Note that entanglements can be released only when they reach a chain end. Thus, the disentanglement process induced by shear flow is going to start in Fig.4b.

In the case of entangled melts, the shear stress $P_{xy}(t)$ and the normal stress $P_{xx}(t) - P_{yy}(t)$ often exhibit overshoot behavior in rapid shearing [9,10,17]. In Fig.5 we show the shear stress $P_{xy}(t)$ and the normal stress difference $P_{xx}(t) - P_{yy}(t)$ after application of shear at $\dot{\gamma} = 10^{-3}$. They were calculated in the same run yielding Fig.4. In agreement with experiments and the previous simulations, (i) these stress components both exhibit a peak around $\dot{\gamma}t \simeq 10$ and afterwards tend to a steady state value and (ii) the peak of $P_{xx}(t) - P_{yy}(t)$ is attained shortly after that of $P_{xy}(t)$. As can be seen in Fig.4b, the chains are stretched without appreciable disentanglement until the stress maximum. We recognize that the stress components begin to decrease with onset of the disentanglement process.

In summary, we have succeeded to detect and visualize the entanglements in a model polymer melt in both quiescent and sheared conditions to obtain $N_e \simeq 80$. This work is supported by Grants in Aid for Scientific Research from the Ministry of Education, Science, Sports and Culture of Japan. Calculations have been performed

at the Human Genome Center, Institute of Medical Science, University of Tokyo and the Supercomputer Center, Institute for Solid State Physics, University of Tokyo.

-
- [1] P.G. de Gennes, *Scaling Concepts in Polymer Physics* (Cornell University, Ithaca, 1979).
 [2] M. Doi and S.F. Edwards, *The Theory of Polymer Dynamics* (Clarendon, Oxford, 1986).
 [3] P. Schleger, B. Farago, C. Lartigue, A. Kollmar, and D. Richter, *Phys. Rev. Lett.*, **81** 124 (1998).
 [4] K. Kremer and G.S. Grest, *J. Chem. Phys.*, **92** 5057 (1990).
 [5] S.W. Smith, C.K. Hall, and B.D. Freeman, *J. Chem. Phys.*, **104** 5616 (1996).
 [6] U. Ebert, A. Baumgärtner, and L. Schäfer, *Phys. Rev. Lett.*, **78** 1592 (1997).
 [7] W. Paul, K. Binder, D.W. Heermann, and K. Kremer, *J.*

- Chem. Phys.*, **95** 7726 (1991).
 [8] M. Pütz, K. Kremer, and G.S. Grest, *Europhys. Lett.*, **49** 735 (2000).
 [9] S. Hess, C. Aust, L. Bennet, M. Kröger, C.P. Borgmeyer, and T. Weider, *Physica A*, **240** 126 (1997).
 [10] T. Aoyagi and M. Doi, *Comp. Theo. Poly. Sci.*, **10** 317 (2000).
 [11] R. Yamamoto and A. Onuki, *J. Phys.; Condens. Matt.*, in print.
 [12] E. Ben-Naim, G.S. Grest, T.A. Witten, and A.R.C. Baljon, *Phys. Rev. E*, **53** 1816 (1996).
 [13] M.P. Allen and D.J. Tildesley, *Computer Simulation of Liquids* (Clarendon, Oxford, 1987).
 [14] D.J. Evans and G.P. Morriss, *Statistical Mechanics of Nonequilibrium Liquids* (Academic, New York, 1990).
 [15] P.H. Verdier, *J. Chem. Phys.*, **45** 2118 (1966).
 [16] We also calculated the time-correlation function of the end-to-end vector $\langle \mathbf{P}(t) \cdot \mathbf{P}(0) \rangle$ and the incoherent dynamic scattering function $S_{inc}(q, t)$. From these data we obtained $\zeta/k_B T \cong 52\tau_0/\sigma^2$ and $b^2 \cong 1.5\sigma^2$ for $10 \leq N \leq 250$.
 [17] D.W. Mead, R.G. Larson, and M. Doi, *Macromolec.*, **31** 7895 (1998).

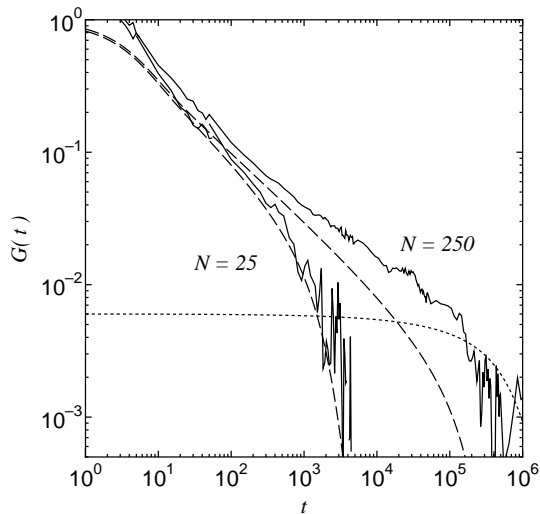


FIG. 1. The calculated stress relaxation function $G(t)$ for $N = 25$ and 250 (solid lines). The Rouse relaxation function $G_R(t)$ (dotted lines) and that from the reptation theory $G_{rep}(t)$ (dashed line) with $N_e = 100$ are also shown.

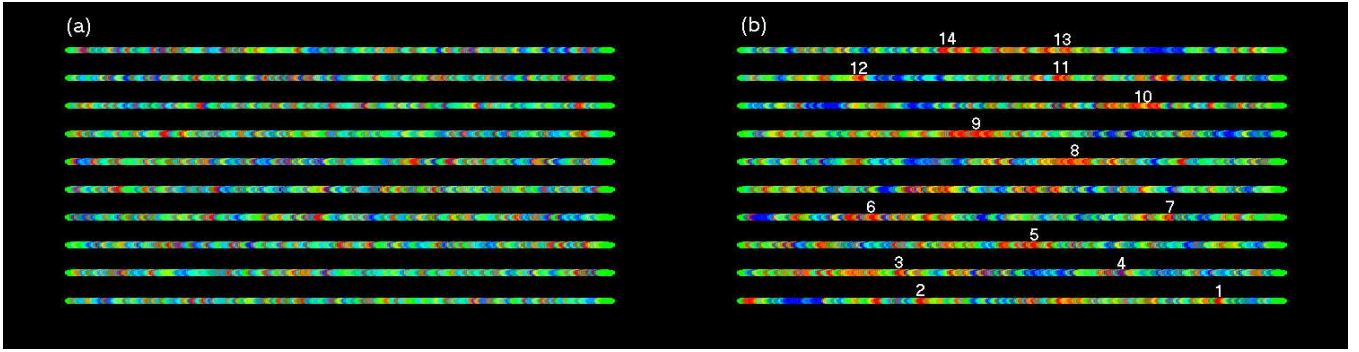


FIG. 2. Distributions of non-bonded interactions on the chains with $N = 250$ in a quiescent state. We can see no correlations along the chains in snapshot values of $[E_i^{\text{NB}}(t) - \langle E^{\text{NB}} \rangle] / \sigma(0)$ in (a). However, the time-averaged normalized interactions $[\bar{E}_i^{\text{NB}}(t) - \langle E^{\text{NB}} \rangle] / \sigma(\tau)$ with $\tau = 5 \times 10^3$ are distinctly strong in line segments consisting of several beads (in red or orange) due to entanglements. Among these segments we number those which keep to hold large non-bonded interaction values during rapid shearing in Fig.4. The color map is the same as in Fig.4.

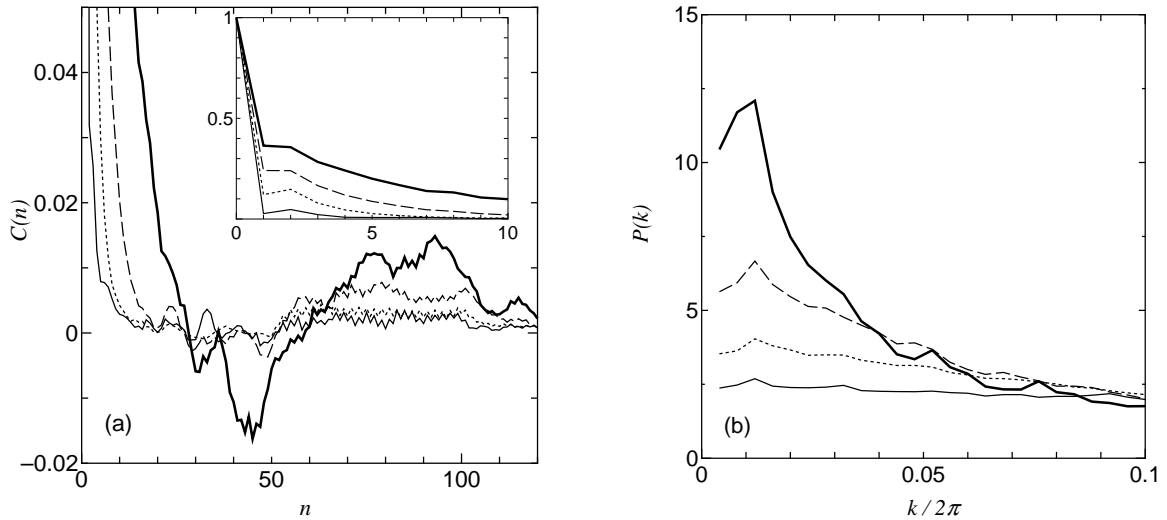


FIG. 3. The auto-correlation function $C(n)$ defined by Eq.(5) in (a), and its power spectrum $P(k)$ defined by Eq.(6) in (b), for various values of the time interval τ . The inset in (a) shows the decay of $C(n)$ for small n . Here $\tau = 0$ (thin-solid line), 5×10 (dotted line), 5×10^2 (dashed line), and 5×10^3 (bold line).

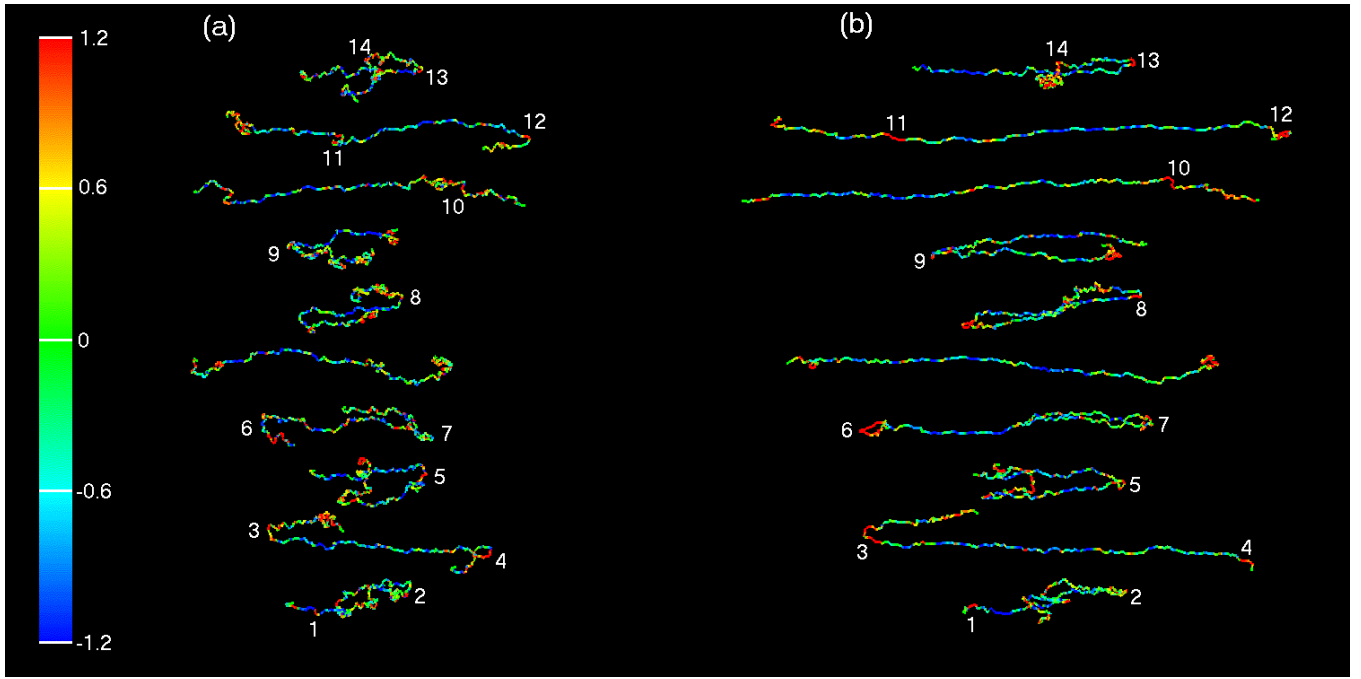


FIG. 4. Snapshots of the deformed chains in the xz plane. A shear flow at $\dot{\gamma} = 10^{-3}$ is applied to the system with the configuration in Fig.2b in the same run. The numbered segments correspond to those in Fig.2b. Here $\dot{\gamma}t = 5$ in (a) and $\dot{\gamma}t = 10$ in (b). The flow is in the horizontal (x) direction, and the shear gradient is in the out-of-plane (y) direction. The non-bonded interactions with $\tau = 500$ are written on the chains. Use is made of the color map on the left, where the numbers are the normalized deviations, $(\bar{E}_i^{NB} - \langle \bar{E}^{NB} \rangle) / \sigma(\tau)$, with $\tau = 500$.

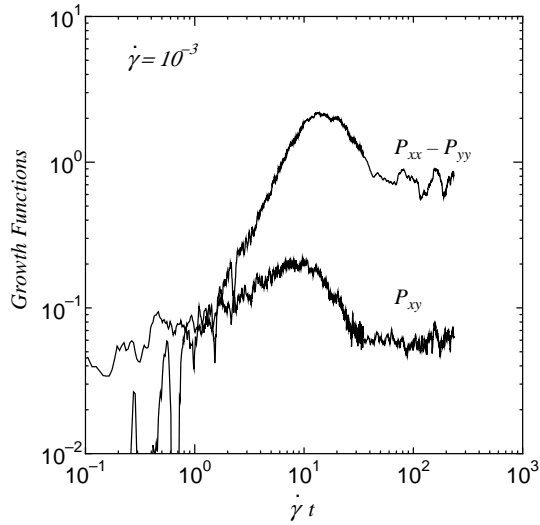


FIG. 5. The stress growth functions after application of shear flow at $\dot{\gamma} = 10^{-3}$ in a model polymer melt with $N = 250$. The chain shapes and entanglements at $\dot{\gamma}t = 10$ are written in Fig.4b.